

# Integral validation of BISON $\text{U}_3\text{Si}_2$ modeling capabilities including multiscale improvements to modeling fission gas behavior

K. A. Gamble<sup>a,\*</sup>, G. Pastore<sup>b</sup>, M. W. D. Cooper<sup>c</sup>, D. A. Andersson<sup>c</sup>, C. Matthews<sup>c</sup>, B. Beeler<sup>d</sup>, L. K. Aagesen<sup>a</sup>, T. Barani<sup>e</sup>, D. Pizzocri<sup>e</sup>

<sup>a</sup>Computational Mechanics and Materials, Idaho National Laboratory, P.O. Box 1625, Idaho Falls, ID 83415-3840, USA

<sup>b</sup>Nuclear Engineering Department, University of Tennessee, Knoxville, TN 37996, USA

<sup>c</sup>MST-8, Materials Science in Radiation and Dynamics Extremes, Los Alamos National Laboratory, P.O. Box 1663, Los Alamos, NM 87545, USA

<sup>d</sup>Nuclear Engineering Department, North Carolina State University, Raleigh, NC 27695-7909, USA

<sup>e</sup>Politecnico di Milano, Department of Energy, Nuclear Engineering Division, Via La Masa 34, 20156 Milano, Italy

## Abstract

Uranium silicide ( $\text{U}_3\text{Si}_2$ ) is a concept explored as a potential alternative to  $\text{UO}_2$  fuel used in light water reactors (LWRs) since it may improve accident tolerance and economics due to its higher thermal conductivity and increased uranium density.  $\text{U}_3\text{Si}_2$  has been previously used in research reactors in the form of dispersion fuel, but operated at lower temperatures than commercial LWRs. The research reactor data illustrated that significant gaseous swelling occurs as the fuel burnup increases. Therefore, it is imperative to understand the fission gas behavior of  $\text{U}_3\text{Si}_2$  under higher temperature LWR operating conditions. In this work, molecular dynamics and phase-field modeling techniques are used to reduce the uncertainty in select modeling assumptions made in developing the fission gas behavior model for  $\text{U}_3\text{Si}_2$  in the BISON fuel performance code. These lower length scale informed models are then utilized in the validation of BISON  $\text{U}_3\text{Si}_2$  modeling capabilities to simulate the ATF-1 experiments irradiated in the Advanced Test Reactor (ATR). Sensitivity analysis (SA) and uncertainty quantification (UQ) are included as part of the validation process to identify where further experiments and lower length scale modeling would be beneficial. The multiscale modeling approach utilized in this work can be applied to new fuel concepts being explored for both LWRs and advanced reactors (e.g., uranium nitride, uranium carbide).

**Keywords:** BISON,  $\text{U}_3\text{Si}_2$ , fission gas behavior, validation, multiscale modeling

## 1. Introduction

The events that unfolded at the Fukushima Daiichi nuclear power plant in March 2011 initiated a significant research effort into alternative materials designed to provide improved accident tolerance compared to the traditional  $\text{UO}_2$ /Zircaloy fuel system used in light water reactors (LWRs). A material is considered to have improved accident tolerance if it results in an increased response time during accident conditions but maintains similar or enhanced performance during normal operation [1].

Uranium silicide ( $\text{U}_3\text{Si}_2$ ) is considered a potential replacement of  $\text{UO}_2$  by both the U. S. Department of Energy's Advanced Fuels Campaign (AFC) and Westinghouse [2] as a means of satisfying the improved accident tolerance definition above due to its higher thermal conductivity; although Westinghouse's interest has dwindled recently. The higher thermal conductivity results in lower fuel centerline temperatures and shallower temperature gradients across the radius of the fuel. The

lower temperature gradients decrease the likelihood of pellet cracking and subsequent radial relocation of the fuel fragments. Another advantage of  $\text{U}_3\text{Si}_2$  is in terms of economics due to its higher uranium density since it may enable higher burnups and longer cycle lengths.

One of the earliest publications on the irradiated behavior of  $\text{U}_3\text{Si}_2$  (Shimizu [3]) was at power reactor temperatures. Until the recent post-irradiation examinations of  $\text{U}_3\text{Si}_2$  by Cappia and Harp [4], Shimizu's work was the only  $\text{U}_3\text{Si}_2$  data at LWR operating temperatures available in the literature. Since then,  $\text{U}_3\text{Si}_2$  has been used in dispersion fuel in research reactors, so the majority of available experimental data is at these lower temperatures. Finlay et al. [5] observed that significant gaseous swelling occurs above a certain burnup associated with the so called "knee" phenomenon. Given the low temperatures of research reactors, the significant swelling was attributed to  $\text{U}_3\text{Si}_2$  being amorphous under irradiation at these temperatures. Birtcher et al. [6] demonstrated that, under high-energy ion irradiation above 250°C,  $\text{U}_3\text{Si}_2$  remains crystalline. This observation was confirmed by Miao et al. [7–9]. LWRs operate well above this threshold, so  $\text{U}_3\text{Si}_2$  is expected to remain crystalline under irradiation in these reactors. Unfortunately, the gaseous fission product behavior and its impact on fuel performance is still not well understood for crystalline  $\text{U}_3\text{Si}_2$  due to the lack of neutron irradiated data at LWR temperatures. Another concern

\*Corresponding author

Email addresses: Kyle.Gamble@inl.gov (K. A. Gamble), gpastore@utk.edu (G. Pastore), cooper\_m@lanl.gov (M. W. D. Cooper), andersson@lanl.gov (D. A. Andersson), cmatthews@lanl.gov (C. Matthews), bwbeeler@ncsu.edu (B. Beeler), Larry.Aagesen@inl.gov (L. K. Aagesen), tommaso.barani@polimi.it (T. Barani), davide.pizzocri@polimi.it (D. Pizzocri)

with  $U_3Si_2$  as a power reactor fuel is its relatively low melting temperature ( $\sim 1938$  K).

The uncertainty associated with fission gas behavior under LWR operating conditions necessitates a mechanistic multiscale modeling approach. In this paper, a review of the models available in the BISON fuel performance code [10] for  $U_3Si_2$  fuel along with their ranges of applicability and uncertainty are summarized. New updates to the parameters of the initial fission gas behavior model developed by [11], based upon molecular dynamics and phase-field analyses, is also presented. The paper concludes with a revisit of a previous validation [12] of the BISON  $U_3Si_2$  modeling capabilities to the recent ATF-1 experiments irradiated in the ATR including sensitivity and uncertainty quantification analyses with the latest versions of the models and estimates of their uncertainty.

## 2. Thermo-mechanical models for $U_3Si_2$

Multiple researchers have used BISON to analyze the fuel performance of  $U_3Si_2$  during normal operating conditions [13, 14]. BISON contains a comprehensive set of thermo-mechanical properties for predicting the fuel performance of  $U_3Si_2$  including thermal conductivity, specific heat, thermal expansion, elasticity, solid swelling, and creep. A coupled fission gas release and swelling model is also available and is described in Section 4.

A review of the already existing models in BISON for thermal conductivity, specific heat, thermal expansion, elasticity, and solid swelling models is provided. New developments in regards to lower length scale improvements in creep and fission gas behavior are also included.

### 2.1. Thermal Properties

BISON contains many options for the thermal conductivity and specific heat capacity of  $U_3Si_2$ . The recommended correlations are those from the  $U_3Si_2$  handbook [15]. The thermal conductivity correlation is a polynomial fit to the data of [3, 16–18]:

$$k = 9.029 \times 10^{-15}T^5 - 4.609 \times 10^{-11}T^4 + 8.676 \times 10^{-8}T^3 - 7.485 \times 10^{-5}T^2 + 4.166 \times 10^{-2}T + 0.5211 \quad (1)$$

where  $T$  is temperature in K. The correlation for the specific heat capacity is given as:

$$C_p = 1000.0 (3.52 \times 10^{-5}T + 0.18) \quad (2)$$

where  $T$  is temperature in K and  $C_p$  is the specific heat capacity in J/kg-K. The uncertainty in the thermal conductivity model is determined by Figure 1, which reproduces a plot similar to the one in the  $U_3Si_2$  handbook [15], with dashed lines to represent the uncertainty assumed in the BISON model. The uncertainty is computed from the experimental data point with the largest deviation from the polynomial fit corresponding to the arc-cast data point at a temperature of  $\sim 1110$  K with a thermal conductivity value of  $\sim 22.5$  W/m-K. This calculation results in a 95%

confidence band of  $\pm 18.2\%$ . It should be noted that the induction cast data of [3] is not included in the uncertainty calculation, due to the measurements significantly underpredicting the thermal conductivity of  $U_3Si_2$ . The uncertainty in the specific heat capacity model is taken as  $\pm 3\%$ , as per [19].

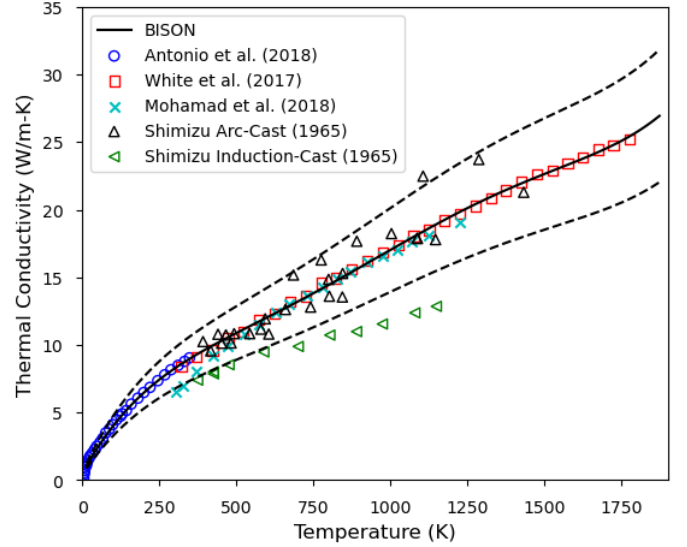


Figure 1: Handbook model with associated uncertainty represented by the dashed lines. Adapted from [15].

### 2.2. Elasticity

For mechanical analyses,  $U_3Si_2$  is treated as an isotropic material. The elastic constants are determined using empirical fits to the data in the  $U_3Si_2$  handbook [15]. The linear fits are illustrated along with the experimental data for the Young's modulus (black) and the shear modulus (blue) in Figure 2. To avoid cluttering the figure, equations of the linear fits are provided below.

The equation for Young's modulus is given by:

$$E = -6.695p + 137.55 \quad (3)$$

where  $E$  is the Young's modulus (GPa) and  $p$  is the porosity (%). The shear modulus is also a porosity-dependent function given by:

$$G = -2.833p + 56.938 \quad (4)$$

where  $G$  is the shear modulus (GPa) and  $p$  is the porosity (%). Once  $E$  and  $G$  are known the Poisson's ratio can be calculated from:

$$\nu = \frac{E}{2.0G} - 1.0 \quad (5)$$

The porosity in percent is calculated from the current density through:

$$p = \left( 1.0 - \frac{\rho_{current}}{\rho_{theoretical}} \right) \times 100\% \quad (6)$$

where  $\rho_{current}$  and  $\rho_{theoretical}$  are the current and theoretical densities of  $U_3Si_2$  respectively. The theoretical density is taken as  $12,200 \text{ kg/m}^3$ , whereas the current density is calculated from the

current fuel volume that takes into account the thermal expansion, creep, solid swelling, densification, and gaseous swelling explained in subsequent subsections.

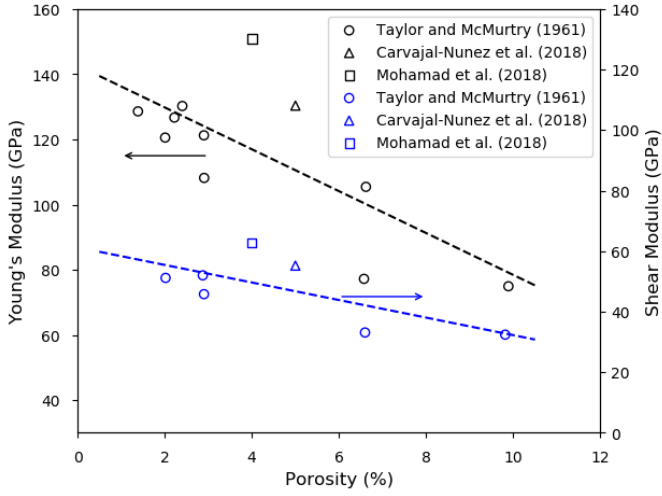


Figure 2: Young's and shear modulus data with trendline. Adapted from [15].

Given the limited amount of data for the elastic properties of  $U_3Si_2$ , the suggested model is designed to capture all of the data points in Figure 2 with a 95% confidence, assuming a normal distribution. Thus, the calculated uncertainty corresponds to two standard deviations about the mean determined by the correlations in Equations 3 and 4. The data points for the Young's ( $\sim 151$  GPa) and shear ( $\sim 63$  GPa) moduli from Mohamad et al. [17] are used to determine the bounds of the model given that it represents the furthest known value from the best-fit correlations. The calculated uncertainty is 29.1% and 26.8% for the Young's modulus and the shear modulus, respectively. Figure 3 illustrates the correlation with the assumed uncertainty over the porosity range for which the model is applicable. Dashed black and blue lines correspond to the uncertainty bands on the Young's modulus and the shear modulus, respectively.

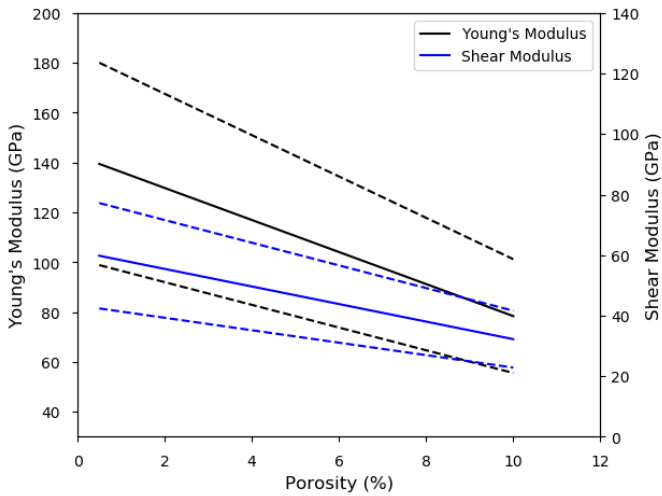


Figure 3: Young's and shear modulus correlations along with their associated uncertainty bands.

### 2.3. Thermal Expansion

The  $U_3Si_2$  handbook provides a temperature-dependent correlation for the instantaneous coefficient of thermal expansion (CTE). However, when including all of the data available for the CTE of  $U_3Si_2$  (see Figure 4) it can be observed that assuming a constant value for all temperatures of  $(16.0 \pm 3.0) \times 10^{-6} K^{-1}$  captures all of the known experimental data. Since the available experimental data on thermal expansion of  $U_3Si_2$  is limited this is the recommended value to use.

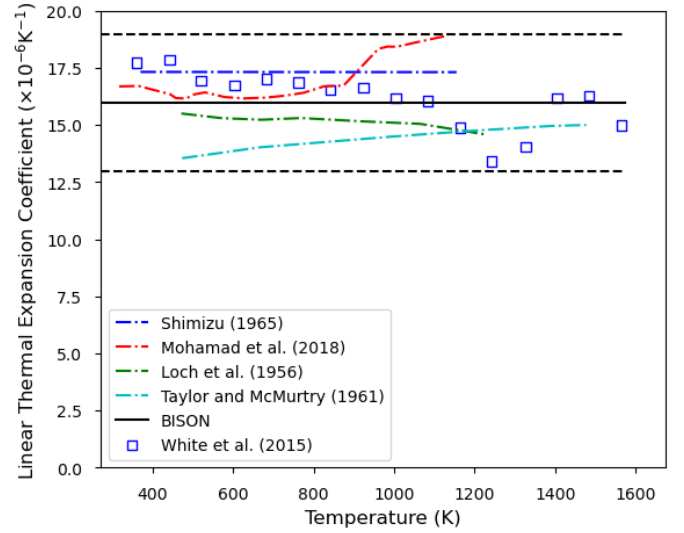


Figure 4: Linear thermal expansion coefficient data with the suggested constant value and uncertainty bands included. Based upon a figure from the  $U_3Si_2$  handbook [15].

### 2.4. Creep

Prior to this work, the creep models for  $U_3Si_2$  were empirical correlations (see [20, 21]) fit to the only experimental data available from the University of South Carolina [22]. Atomistic calculations were performed to develop a creep model containing contributions from three mechanisms of creep: Coble, Nabarro-Herring, and dislocation climb. The details on the derivation of the creep model can be found in [23]. Here, the final equations (as implemented into BISON) are shown.

The total creep rate is given by:

$$\dot{\epsilon} = \dot{\epsilon}_{NH} + \dot{\epsilon}_{Coble} + \dot{\epsilon}_{Climb} \quad (7)$$

where  $\dot{\epsilon}_{NH}$ ,  $\dot{\epsilon}_{Coble}$ , and  $\dot{\epsilon}_{Climb}$  are the contributions from Nabarro-Herring, Coble, and dislocation climb mechanisms, respectively ( $s^{-1}$ ). The Nabarro-Herring creep rate is given by:

$$\dot{\epsilon}_{NH} = \frac{\sigma}{d^2 T} \left[ 1.457 \times 10^{-11} \exp\left(\frac{-3.400}{k_B T}\right) + 5.081 \times 10^{-51} \dot{F} \exp\left(\frac{-0.540}{k_B T}\right) + 5.912 \times 10^{-14} \exp\left(\frac{-3.390}{k_B T}\right) \right] \quad (8)$$

where  $\sigma$  is the effective stress (Pa),  $T$  is the temperature (K),  $d$  is the grain size (m),  $k_B$  is the Boltzmann constant (eV/K) and  $\dot{F}$  is the fission rate density ( $\text{m}^3/\text{s}$ ). Similarly, the Coble creep rate is given by:

$$\dot{\epsilon}_{\text{Coble}} = \frac{\sigma}{d^3 T} 7.294 \times 10^{-20} \exp\left(\frac{-1.619}{k_B T}\right) \quad (9)$$

For dislocation climb the creep rate is:

$$\dot{\epsilon}_{\text{Climb}} = \frac{\sigma^3}{T} \left[ 1.512 \times 10^{-11} \exp\left(\frac{-4.160}{k_B T}\right) + 4.696 \times 10^{-55} \dot{F} \exp\left(\frac{-0.020}{k_B T}\right) \right] \quad (10)$$

The uncertainty in the lower length scale informed creep model is unknown. The model is included in the validation studies completed in this work, but it is not treated as an uncertain input.

### 2.5. Solid Swelling

The total volumetric change due to swelling of the fuel is comprised of three components: solid and gaseous swelling, and densification. The behavior of solid fission products at LWR operating temperatures is expected to be similar to that at research reactor temperatures. Therefore, the solid swelling model in BISON is based upon the data from Hofman [24]. Hofman's data shows solid swelling as a function of the fission density in units of fissions/ $\text{cm}^3$ . To convert from fission density to units of burnup in fissions per initial metal atom (FIMA) (the units used in BISON), the fission density values are multiplied by a conversion factor of  $3.635 \times 10^{-23} \text{ cm}^3/\text{fission}$ . After conversion, the correlation used is given by:

$$\left(\frac{\Delta V}{V}\right)_{\text{solid}} = 0.34392 Bu \quad (11)$$

where  $(\Delta V/V)_{\text{solid}}$  is the volumetric strain due to solid fission products and  $Bu$  is the burnup in FIMA. The uncertainty in solid swelling is assumed to be the same as for  $\text{UO}_2$ , given the fact that the correlation is also a linear function of burnup. This uncertainty is assumed to be  $\pm 20\%$  [25].

### 2.6. Densification

The densification behavior of  $\text{U}_3\text{Si}_2$  is unknown. It is expected to be different than  $\text{UO}_2$  contrary to [13]. Since no model exists, densification has been ignored in this work.

## 3. Development of the Fission Gas Diffusivity Model

Diffusion in nuclear fuel can exhibit three regimes: i) intrinsic diffusion at high temperatures ( $D_1$ ), ii) irradiation-enhanced diffusion at intermediate temperatures ( $D_2$ ), and iii) athermal diffusion at low temperatures ( $D_3$ ).  $D_1$  is thermally activated diffusion where defects are at thermal equilibrium concentrations.  $D_2$  is due to thermal hopping of defects that have irradiation enhanced concentrations.  $D_3$  is caused by atomic mixing

during irradiation damage events. Due to a lack of experimental data for  $\text{U}_3\text{Si}_2$ , lower length scale (LLS) simulations have been used, in this work, to study diffusivity of fission gas under irradiation conditions. Andersson et al. [26] used DFT to calculate the diffusion coefficients for a range of Xe-containing defects in  $\text{U}_3\text{Si}_2$ . That work focused on diffusion under thermal equilibrium ( $D_1$ ) but, in doing so, generated all of the necessary data for cluster dynamics simulations of irradiation enhanced diffusion.

### 3.1. Centipede

To study irradiation-enhanced diffusivity in  $\text{U}_3\text{Si}_2$ , cluster dynamics simulations have been used to predict the steady state concentration of defects. In previous work [23], we used the Centipede code to simulate irradiation-enhanced self-diffusion of U and Si based on Frenkel production due to irradiation, annihilation at sinks, and mutual recombination. Here we build upon that model by including Xe-containing defect clusters. Although the Centipede code has been discussed in detail elsewhere [27, 28], here we give a brief overview of the methodology for completeness.

The concentrations of defects in the system are calculated by solving a set of ordinary differential equations (ODEs) that capture a number of phenomena including: production of Frenkel pairs through irradiation, mutual recombination of Frenkel pairs, interaction with sinks, and clustering of point defects. For a given defect concentration,  $x_d$ , the ODE can be expressed as:

$$\frac{dx_d}{dt} = \dot{\beta}_d + \sum_C \dot{R}_{d,C}(x_d, x_C, T, G) - \sum_s \dot{S}_{d,s}(x_d, x_s, T, G) \quad (12)$$

where  $\dot{\beta}_d$  describes the source rate of defects through radiation damage.  $\dot{R}_{d,C}$  and  $\dot{S}_{d,s}$  are the cluster and sink rates, which are summed across individual cluster and sink types, respectively. The Centipede code finds the steady-state solution to this coupled set of ODEs, such that  $\frac{dx_d}{dt} \leq \mathcal{R}$  for all defects, where  $\mathcal{R}$  is a convergence criteria. An individual reaction rate,  $\dot{R}_d$ , can be expressed as:

$$\dot{R}_d = \begin{cases} \frac{k_f^2}{\Omega} D x_A x_B \left[ 1 - \exp\left(\frac{f}{k_B T}\right) \right], & \text{if } f < 0, \\ \frac{k_r^2}{\Omega} D x_Y x_Z \left[ \exp\left(\frac{f}{k_B T}\right) - 1 \right], & \text{otherwise} \end{cases} \quad (13)$$

where  $\Omega$  is the atomic volume,  $k_i$  is a reaction rate constant,  $D = D_A + D_B$  is the sum of the diffusivities of the reactants (labeled A and B),  $x_A$  and  $x_B$  are the concentrations of the reactants and  $x_Y$  and  $x_Z$  are the concentrations of the products (labeled Y and Z). If  $f < 0$  the net rate is for the reaction to go forwards and otherwise it goes backwards. The driving force is given by the change in the free energy of the system due to the reaction:

$$f = \sum_{p \in P} \frac{\partial G}{\partial x_p} - \sum_{r \in R} \frac{\partial G}{\partial x_r} \quad (14)$$

where  $P$  and  $R$  are the set of products,  $p$ , and reactants,  $r$ , respectively. A detailed explanation of Eqs. (12) to (14) and their

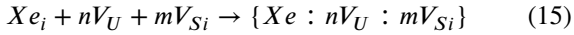
Table 1: Point defect formation energies and entropies, and the cluster binding energies and entropies, from Andersson et al. [26], used in the cluster dynamics model.

| Point Defect            | $H_f$ (eV) | $S_f$ ( $k_B$ ) | $n$ |
|-------------------------|------------|-----------------|-----|
| $U_i$                   | 0.87       | -3.15           | 2   |
| $V_U$                   | 1.69       | 0.45            | 1   |
| $Si_i$                  | 0.55       | 2.19            | 1   |
| $V_{Si}$                | 1.79       | 6.28            | 2   |
| Cluster                 | $H_B$ (eV) | $S_B$ ( $k_B$ ) | $n$ |
| $Xe_U$                  | -2.12      | -1.88           | 1   |
| $Xe_{Si}$               | -2.10      | -9.32           | 1   |
| $\{Xe : 2V_U\}$         | -2.61      | -2.59           | 1   |
| $\{Xe : 2V_{Si}\}$      | -2.05      | -9.32           | 1   |
| $\{Xe : V_U : V_{Si}\}$ | -3.35      | -4.19           | 1   |

application to  $UO_2$  is given in by Matthews et al. [27, 28].

### 3.2. Cluster dynamics simulations for $D_1$ and $D_2$

The total concentration of Xe in the lattice is governed by the processes of fission (sourcing), and trapping and resolution at intra-granular bubbles. These processes are not considered within the Centipede code but are instead taken into account by the fission gas release model within BISON. The concentration of Xe in the lattice is, thus, treated as fixed during the cluster dynamics simulations. As such, the absolute formation energies of the Xe-containing defects do not influence the end results; instead, the relative energies are only considered. The reference Xe-containing defect has been taken to be a Xe interstitial,  $Xe_i$ . All other Xe-containing defects (e.g.  $Xe_U$  and  $Xe_{Si}$ ) have been treated as clusters, whereby the binding energy with respect to the constituent point defects is used within the Centipede code. The following reaction defines the binding energy:



where  $n$  and  $m$  are the number of  $V_U$  and  $V_{Si}$  point defects that make up the cluster, and standard Kröger-Vink notation has been used, except with charges omitted due to the metallic-bonding of  $U_3Si_2$ . Clusters consisting of more than one vacancy are denoted using braces. For example,  $\{Xe : V_U : V_{Si}\}$  represents a cluster containing one U vacancy, one Si vacancy, and a Xe atom but without specifying the exact site that Xe occupies within the vacancy cluster.

The binding energies,  $H_B$ , and entropies,  $S_B$ , for all defect clusters considered are determined from the data in Andersson et al. [26] and are summarized in Table 1, alongside the point defect formation energies,  $H_f$ , and entropies,  $S_f$ . Negative and positive values for the binding energy and entropy, respectively, contribute to favorable binding.

The parameters in Table 1 govern the stability of defects under thermal equilibrium. However, the diffusivity of the defects is also critical to modeling the irradiation enhanced concentrations of defects. The diffusivity of a defect,  $x$ , is given by:

$$D_x = \frac{Z}{2\xi} \alpha^2 v_{mig} \exp\left(\frac{-H_{mig}}{k_B T}\right) \quad (16)$$

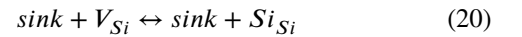
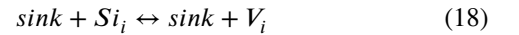
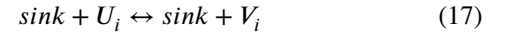
Table 2: Parameters that describe the point defect and cluster diffusivities, from Andersson et al. [26], used in the cluster dynamics model. The impurity defect  $Xe_U$  and  $Xe_{Si}$  are immobile and are, as such, omitted.

| Point Defect            | $H_{mig}$ (eV) | $v_{mig}$ (Hz)        | $\alpha$ (Å) | $\xi$ | $Z$ |
|-------------------------|----------------|-----------------------|--------------|-------|-----|
| $U_i$                   | 0.31           | $1.51 \times 10^{14}$ | 3.80         | 2     | 4   |
| $V_U$                   | 1.21           | $1.40 \times 10^{13}$ | 3.90         | 1     | 2   |
| $Si_i$                  | 1.80           | $1.00 \times 10^{13}$ | 5.18         | 2     | 4   |
| $V_{Si}$                | 2.37           | $1.00 \times 10^{13}$ | 4.19         | 2     | 4   |
| $Xe_i$                  | 3.13           | $1.00 \times 10^{14}$ | 3.90         | 1     | 2   |
| Cluster                 | $H_{mig}$ (eV) | $v_{mig}$ (Hz)        | $\alpha$ (Å) | $\xi$ | $Z$ |
| $\{Xe : 2V_U\}$         | 1.68           | $1.00 \times 10^{13}$ | 3.90         | 1     | 2   |
| $\{Xe : 2V_{Si}\}$      | 2.33           | $1.00 \times 10^{13}$ | 4.19         | 2     | 4   |
| $\{Xe : V_U : V_{Si}\}$ | 2.61           | $1.00 \times 10^{13}$ | 4.19         | 2     | 4   |

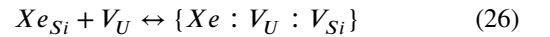
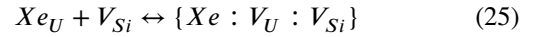
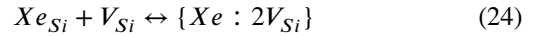
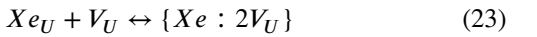
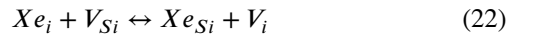
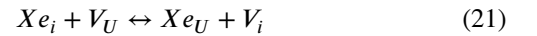
where  $H_{mig}$  is the defect migration barrier,  $v_{mig}$  is the attempt frequency,  $Z$  is the number of jump directions,  $\alpha$  is the jump distance, and  $\xi$  is the dimensionality of diffusion. Diffusion in  $U_3Si_2$  is highly anisotropic due to the tetragonal crystal structure. However, if two point defects come into contact the subsequent reaction is agnostic of the crystallographic direction that the defect arrived from. Therefore, the defect reactions that are being solved for will be dominated only by diffusion in the fastest direction. The parameters for diffusion in the fastest direction for each defect, as used in Centipede, are taken from Andersson et al. [26] and are summarized in Table 2.

The parameters for defect stability and diffusion were implemented in the Centipede code to determine the irradiation enhanced defect concentrations for Xe-containing clusters in  $U_3Si_2$ . When solving for the steady-state concentrations, the following defect reactions were included:

*Reactions of U and Si defect with sinks*

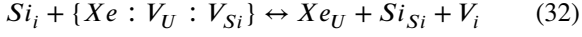
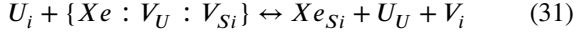
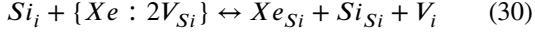
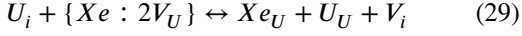
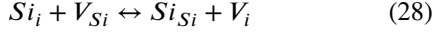
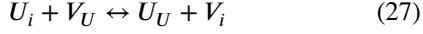


*Binding reactions*

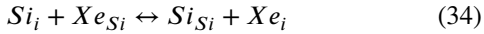
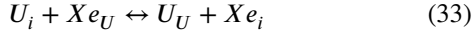




### Recombination of interstitials and vacancies



### Kickout reactions



The system was evolved using the Centipede code until it reached steady-state, whereby the rate of change of all defect concentrations, due to the above reactions, tends to zero. When determining the diffusivity of Xe, the relative concentration of each defect is the parameter of interest, rather than the absolute concentration, which is solved separately based on interactions of Xe with intra-granular bubbles. Figure 5 shows the relative concentrations of Xe-containing clusters in  $U_3Si_2$ . For comparison, the thermal equilibrium relative concentrations are also shown using dashed lines. It can be seen that there is very limited irradiation-enhancement of defect concentrations over a wide range of temperatures. In fact, for all defects other than a Si di-vacancy containing a Xe atom,  $\{Xe : 2V_{Si}\}$ , the irradiation enhancement is negligible over the full temperature range that has been studied (600 – 1500 K).

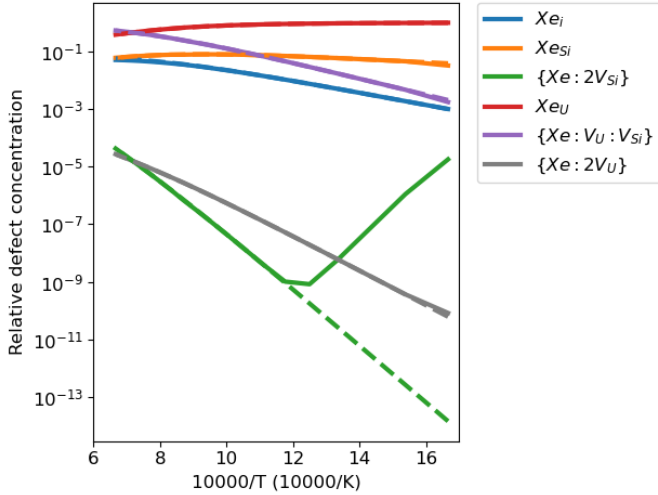


Figure 5: The relative concentrations of various Xe-containing defects in  $U_3Si_2$  under-irradiation predicted by cluster dynamics simulations. The irradiation-enhanced and thermal equilibrium results are shown by solid and dashed lines, respectively.

Figure 6 shows the contribution to total Xe diffusivity due to various Xe-containing defects under-irradiation. This is determined by multiplying the relative concentration of a given defect (shown in Fig. 5) by the diffusivity of that defect, as defined by

the data in Table 2. Similarly to the results shown in Fig. 5, there is no enhanced-diffusivity for any defects, except  $\{Xe : 2V_{Si}\}$ , which is enhanced below 850 K. However,  $\{Xe : 2V_{Si}\}$  does not dominate diffusivity above 600 K and, therefore, irradiation-enhanced  $D_2$  diffusion is not expected to dominate at temperatures experienced in LWRs.

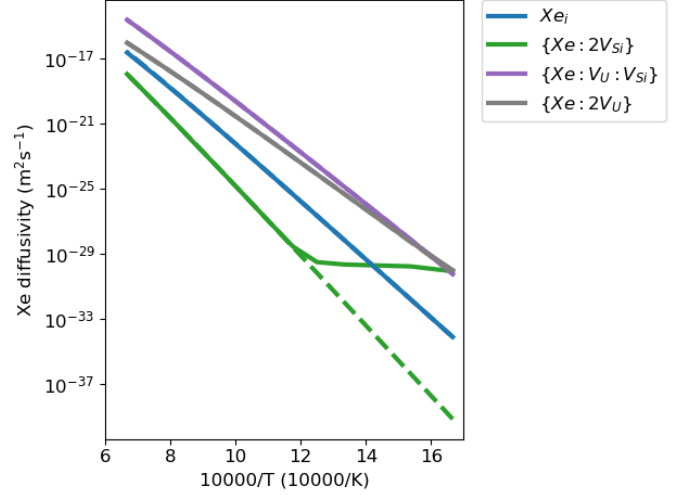


Figure 6: The diffusivity of various Xe-containing defects in  $U_3Si_2$  under-irradiation predicted by cluster dynamics simulations. The irradiation-enhanced and thermal equilibrium results are shown by solid and dashed lines, respectively.

### 3.3. MD simulations of $D_3$

While we do not expect a  $D_2$  contribution to Xe diffusivity, we must still consider the possibility of the athermal  $D_3$  contribution, which is caused by atomic mixing during damage events. To investigate this, MD simulations were carried out using the Large-scale Atomic/Molecular Massively Parallel Simulator (LAMMPS) code [29] with the interatomic forces for  $U_3Si_2$  and Xe in  $U_3Si_2$  given by the MEAM potential of Beeler et al. [30, 31]. A  $30 \times 30 \times 30$  supercell of  $U_3Si_2$ , where 1% of the U atoms were replaced with Xe, was equilibrated at 600 K for 15 ps in the NPT ensemble, with the supercell dimensions averaged over the final 5 ps. By fixing the supercell geometry at the averaged values, MD simulations of ballistic cascades were carried out in the NVE ensemble using PKA energies of 1 keV, 2 keV, and 3 keV. As discussed previously, very small timesteps had to be used to ensure conservation of energy during the simulation. This made it too difficult to carry out simulations of PKA energies greater than 3 keV. A 0.001 fs timestep was used for the first 0.5 ps, followed by 0.003 fs for 3 ps, then 0.01 fs for 10 ps, and 0.1 fs for the remaining 16.5 ps. The simulations were repeated three times for each energy using a random orientation for the PKA velocity each time.

During the simulations the mean squared displacement (MSD) of the Xe atoms was computed. Figure 7 shows the MSD as function of time for Xe, U, and Si during a 3 keV cascade. The data for U and Si are from a similar study by Cooper et al. [23], whereas the Xe data was calculated here. For all species there

is an initial rapid increase in the MSD, followed by some oscillations that eventually settle. For the 3 keV cascade shown in Fig. 7, the Xe atoms were displaced less significantly than the U and Si atoms.

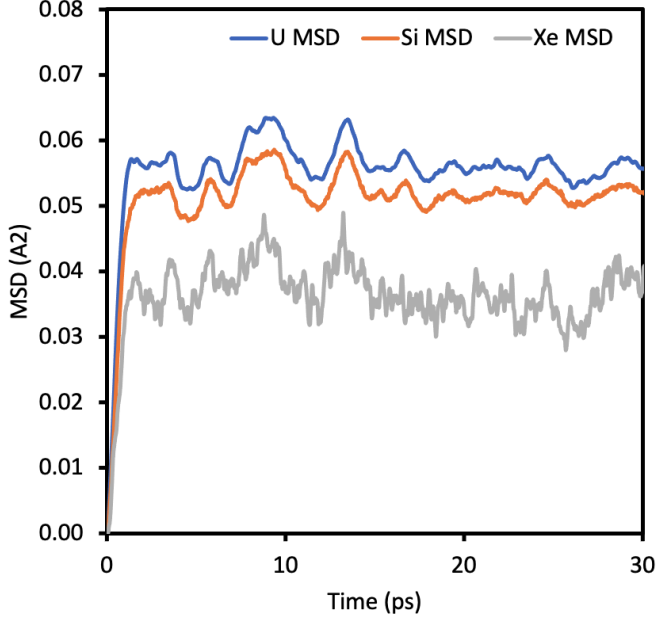


Figure 7: The MSD of Xe (gray) as a function of time during a ballistic cascade in  $U_3Si_2$ . The data from a similar cascade simulation carried out by Cooper et al. [23] for U (blue) and Si (orange) in  $U_3Si_2$  are included for comparison.

For a given PKA energy, the final MSD is taken by averaging over the final 16 ps of each simulation and then averaging again over three such cascade simulations. The MSD is shown as a function of the PKA energy per unit supercell volume in Fig. 8. It can be seen that Xe is displaced to a lesser extent than either U or Si for all PKA energies considered; except the 1 keV cascades, where it is displaced marginally more than Si. Therefore, the athermal diffusivity in  $U_3Si_2$  due to ballistic mixing is expected to be lower for Xe than for U or Si.

The slope of the data in Fig. 8 defines the extent of atomic mixing for given amount of energy deposited by a PKA. In nuclear fuel, high energy fission fragments deposit energy into the lattice through damage cascades (ballistic stopping) and thermal spikes (electronic stopping). Both of these processes could, in principle, contribute to the athermal diffusion coefficient:

$$D_3 = D_B + D_E \quad (35)$$

where  $D_B$  and  $D_E$  are the contributions to athermal diffusion from ballistic and electronic stopping, respectively. We assume that, unlike in  $UO_2$  (an insulator), energy deposited electronically in  $U_3Si_2$  (metal-like) is rapidly dissipated due to the high electronic thermal conductivity of the system [19]. Therefore, we consider energy deposited electronically as not contributing to atomic mixing. Instead, only the remaining 10% of energy that is deposited ballistically contributes to athermal diffusion, such that, following a similar approach to that carried previously

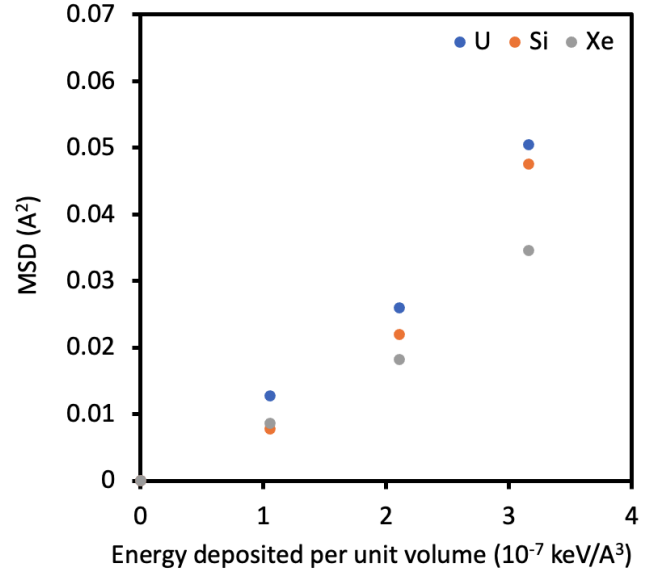


Figure 8: The MSD of Xe (gray) averaged over the final 15 ps of cascade simulations at 600 K as a function of PKA energy deposited per unit volume. The data from Cooper et al. [23] for U (blue) and Si (orange) are included for comparison.

on other fuels [32, 33]:

$$D_3 = A\dot{F} \quad (36)$$

$$A = \frac{0.1}{6}\epsilon_B E_F \quad (37)$$

where  $\dot{F}$  is the fission rate per unit volume, and  $A$  is the constant of proportionality between  $D_3$  and  $\dot{F}$ .  $\epsilon_B$  is the MSD per unit energy deposited in a unit volume of lattice due to ballistic damage cascades, which is determined by the slope of a linear fit to the data in Fig. 8. The factor of 1/6 accounts for diffusion in three dimensions, given that the directions of PKAs due to ballistic stopping are randomized. The energy released due to a single fission event,  $E_F$ , is taken as 170 MeV. The factor of 0.1 accounts for the fact that, as discussed previously, only 10% of  $E_F$  is deposited ballistically in  $U_3Si_2$  (based on the value for UC being representative of  $U_3Si_2$ , using the same assumption as in Matthew et al. [34]).

Table 3 shows the values of  $E_B$ ,  $A$ , and  $D_3$  for Xe in  $U_3Si_2$  based on a typical  $\dot{F}$  of  $10^{19} \text{ m}^{-3}\text{s}^{-1}$  for LWR conditions. For comparison, the values for U and Si from Cooper et al. [23] are also shown. As already discussed in relation to Figs. 7 and 8, Table 3 shows  $D_3$  is lower for Xe than it is for U or Si. More importantly,  $D_3$  for Xe is higher by several orders of magnitude than irradiation-enhanced diffusion ( $D_2$ ), as determined from cluster dynamics (Section 3.2). Therefore, the diffusivity of Xe for in-reactor conditions can be described over a wide temperature range by  $D_1$  and  $D_3$  contributions only.

Table 3: The  $\epsilon_B$ ,  $A_B$ , and  $D_3$  parameters for Xe in  $U_3Si_2$ .  $E_F$  is taken to be 170 MeV and it is assumed 10 % of this energy is deposited through ballistic stopping.  $D_3$  values assume a fission rate density of  $10^{19} \text{ m}^{-3}\text{s}^{-1}$ . These assumptions can be modified depending on reactor design or local irradiation conditions.

| Species | $\epsilon_B \text{ (m}^5\text{MeV}^{-1}\text{)}$ | $A_B \text{ (m}^5\text{)}$ | $D_3 \text{ (m}^2\text{s}^{-1}\text{)}$ |
|---------|--|----------------------------|---|
| U [23]  | $1.46 \times 10^{-42}$                           | $4.15 \times 10^{-42}$     | $4.15 \times 10^{-23}$                  |
| Si [23] | $1.32 \times 10^{-42}$                           | $3.73 \times 10^{-42}$     | $3.73 \times 10^{-23}$                  |
| Xe      | $1.01 \times 10^{-42}$                           | $2.86 \times 10^{-42}$     | $2.86 \times 10^{-23}$                  |

*Stoichiometric conditions:*

$$D_{Xe} = D_1 + D_3 \quad (38)$$

$$D_{Xe} = 4.82 \times 10^{-5} \exp\left(\frac{-3.04}{k_B T}\right) + 2.86 \times 10^{-42} \dot{F} \quad (39)$$

This LLS-informed Xe diffusion coefficient has been used to inform a stoichiometric  $U_3Si_2$  fission gas swelling and release model, as described in Section 4. Given the extremely high energy nature of ballistic cascades, we have assumed that  $D_3$  is insensitive to changes in chemistry, whereas for  $D_1$  a modification can be provided based on the results from Andersson et al. [26] to account for Si-rich conditions. U-rich conditions have been omitted given that Middleburgh et al. only predicted significant deviation from stoichiometric  $U_3Si_2$  on the Si-rich side of the phase diagram [35].

*Si-rich conditions:*

$$D_{Xe} = 7.22 \times 10^{-6} \exp\left(\frac{-2.84}{k_B T}\right) + 2.86 \times 10^{-42} \dot{F} \quad (40)$$

#### 4. Gaseous Swelling and Fission Gas Release

The BISON model for fission gas behavior in  $U_3Si_2$  incorporates the fundamental physical mechanisms of fission gas behavior and calculates the coupled fission gas release (FGR) and gaseous swelling concurrently. Given the lack of experimental data for  $U_3Si_2$  under LWR conditions, a multiscale approach has been adopted for model development, with the engineering BISON model being informed by parameters calculated via atomistic and meso-scale simulations. Considering that  $U_3Si_2$  under LWR conditions retains a polycrystalline structure, fission gas behavior is modeled as consisting of two main stages (intra-granular and inter-granular behavior) analogous with  $UO_2$ . Correspondingly, the model includes components for the intra-granular and inter-granular behavior of fission gases. The intra-granular component is based on a reduced-parameter cluster dynamics model and computes the evolution of intra-granular fission gas bubbles and swelling coupled with gas diffusion to grain boundaries. The inter-granular component describes the evolution of grain-boundary fission gas bubbles coupled to fission gas release, based on the approach developed for  $UO_2$  in [36], modified by the usage of specific  $U_3Si_2$  parameters. The current BISON model is based on the development described in [11]. However, improvements have been made in the present version,

based on recent lower length scale calculations. In particular, these include atomistic calculations to better assess the diffusion coefficients of fission gas atoms and vacancies in  $U_3Si_2$ . The latest model, applied in the present work, also includes improved parameters based on molecular dynamics calculations in [37] and the phase-field calculations of [38].

The molecular dynamics calculations by [37] determined an improved value for the surface energy of  $1.7 \pm 0.85 \text{ J/m}^2$ . Also, based on [37], an improved estimate for the semi-dihedral angle of lenticular grain-boundary fission gas bubbles,  $\theta$ , was developed as  $\theta = 73^\circ$ . The uncertainty on the semi-dihedral angle is assumed to be a uniform scaling factor between 0.5 and 1.0. This is to ensure that the uncertainty range does not extend towards the unrealistic theoretical value of  $90^\circ$  while still bounding the nominal value for  $UO_2$  of  $50^\circ$  used in previous studies [12]. The phase-field calculations by [38] calculated a more realistic value of  $0.6 \pm 0.072$  for the fractional coverage of grain boundaries, known as  $F_{c,sat}$ . The uncertainties in both the surface energy and saturation coverage are assumed to be 95% confidence (i.e., two standard deviations).

Atomic scale simulations have been used to investigate irradiation-enhanced Xe diffusivity in Section 3 combined with the thermal equilibrium data from Andersson et al. [26]. Equations (39) and (40) for the unperturbed fission gas diffusivity can be implemented directly into the fission gas release model in BISON. Due to the inclusion of Xe athermal diffusion in Eqs. (39) and (40), the model can be applied over a wide range of temperatures and fission rates.

Another important component of the fission gas release model is the diffusion of vacancies to inter-granular bubbles that enable the bubbles to swell and reach their equilibrium pressure. Building upon the thermal equilibrium DFT study of Andersson et al. [26], Cooper et al. [23] examined the irradiation-enhanced diffusivity for U and Si defects in  $U_3Si_2$  in the context of self-diffusion and creep. They found that for all temperatures the diffusivity of  $V_{Si}$  was lower than that of  $V_U$ . Given that stoichiometry must be maintained for significant bubble growth to occur, this makes  $V_{Si}$  the rate limiting process for inter-granular bubble swelling. Note that  $D_3$  is excluded from vacancy diffusion since the disorder during a cascade means that tracking the displacement of individual vacancies loses its meaning. Instead the second term in Eqs. (41) and (42) is due to the irradiation enhanced  $D_2$  regime.  $D_1$  and  $D_2$  have been determined by fitting to literature data for  $V_{Si}$  [23].

*Stoichiometric conditions:*

$$D_{ig}^v = 9.72 \times 10^{-4} \exp\left(\frac{-4.16}{k_B T}\right) + 1.97 \times 10^{-47} \dot{F} \quad (41)$$

where  $D_{ig}^v$  represents the Si vacancy diffusivity in  $\text{m}^2/\text{s}$  and  $\dot{F}$  is the fission rate density in  $\text{fissions/m}^3\text{-s}$ .  $k_B T$  is the Boltzmann constant in eV/K. Similarly to Xe diffusion, the  $D_1$  contribution is sensitive to changes in chemistry and, as such, based on the data from Andersson et al. [26],  $D_1$  has been adjusted for Si-rich conditions.



*Si-rich conditions:*

$$D_{ig}^v = 9.76 \times 10^{-5} \exp\left(\frac{-4.22}{k_B T}\right) + 1.97 \times 10^{-47} \dot{F} \quad (42)$$

## 5. Validation and Sensitivity Analysis

The only experimental data available to validate the  $U_3Si_2$  models in BISON at LWR temperatures are the two rods that underwent PIE from the Advanced Test Reactor (ATR) irradiations. PIE has been completed on two rods identified as R4 from the ATF-13 capsule and R6 from the ATF-15 capsule [4]. The experiments are a typical capsule irradiation test, consisting of a fuel rodlet encapsulated inside a stainless-steel capsule. The nominal dimensions of all capsules used in the ATF-1 experiments are shown in Figure 9. Specific details for the R4 and R6 rodlets can be obtained from the design specifications for the experiments. The R4 and R6 rodlets consisted of 12 enriched (5.4 4wt% U-235)  $U_3Si_2$  pellets stacked on top of a single depleted pellet with an additional two depleted pellets placed on top of the active length. The top two depleted pellets were drilled to accommodate melt wires to monitor the temperature during the experiments. In these experiments, the fuel was placed inside ZIRLO<sup>TM</sup> cladding before being inserted into the stainless-steel capsule. Details on the fabrication of the fuel pellets used in these experiments are discussed in [39].

The power supplied to the fuel rodlets as a function of time is shown in Figure 10. A flat axial profile was assumed in the BISON simulation given the short length of the rodlet. The rodlets were removed from the ATR at a relatively low burnup (17.1 MWd/kgHM for R4 and 19.6 MWd/kgHM for R6 [4]) to perform PIE. For engineering scale simulation comparisons, limited data exists. Previous experience from research reactor irradiations of  $U_3Si_2$  suggested that, at some point, the fuel will experience runaway swelling [5]. Therefore, measurements focused on dimensional changes of the fuel and cladding, as well as fission gas release. Measurements of fuel dimensional changes were limited to neutron radiography, which illustrated that the fuel experienced no axial growth (elongation) within the resolution of the measurement technique. Cladding profilometry measurements indicated negligible changes from the as-fabricated dimensions, meaning that no contact between the fuel and cladding was observed [4].

A full uncertainty quantification (UQ) and sensitivity study was completed. Table 4 presents the range of applicability, uncertainty, and references for all of the  $U_3Si_2$  models available in BISON as described in Sections 2 and 4. The uncertainties are assumed to represent two standard deviations for the normal distributions. For the uniform and loguniform distributions, any and all values between the upper and lower limits of the range are possible. In the table,  $T$  is the temperature and  $p$  is the porosity. Further details on the form of the equations and the determination of their uncertainty can be found in [12]. It should be noted that, based upon [41], the grain growth in  $U_3Si_2$  can be ignored. In addition, as mentioned in Section 2.6, densification has been neglected in this study, contrary to previous investigations [12, 13].

To perform the study, the finite element mesh of the drop-in capsule was created using a 2D-RZ axisymmetric smeared pellet mesh assumption. This means that there is an azimuthal plane of symmetry about the rodlet centerline, and the dish and chamfer features of the fuel are not modeled. The insulator pellets – one at the bottom of the stack and two at the top – were included in addition to the ZIRLO<sup>TM</sup> cladding and stainless-steel capsule. Eleven finite elements were used across the radius of the fuel pellet, with four each through the thickness of the cladding and capsule. Three axial elements per pellet were used, with the cladding and capsule meshes being slightly coarser to ensure improved robustness of the contact algorithm.

The UQ and SA studies were performed by coupling BISON to the Dakota [43] software developed at Sandia National Laboratories. A Latin hypercube sampling (LHS) technique was used to reduce the number of samples required. Two-thousand samples were run for two separate studies, the first using the stoichiometric diffusivities for Xe atoms and Si vacancies, and the second using the Si-rich diffusivities. The results of study are presented in Table 5 and Figures 11 and 12.

Table 5 presents the results of the uncertainty quantification analysis. The BISON results are presented as the minimum to maximum value of fuel elongation and fission gas release, assuming one standard deviation about the mean value. The results indicate that BISON predicts a small, non-zero axial change in the fuel stack. While the uncertainty range does not encompass the experimental measurement of zero axial change, it should be noted that the uncertainty of the neutron radiography technique is likely large enough to overlap with the model uncertainty. In addition, recall that a densification model was not included in the BISON analyses, due to the unknown nature of the mechanism in  $U_3Si_2$ . If such a model were to be added, it would serve to reduce the total amount of fuel elongation. For fission gas release, it is observed that the experimental values are captured within uncertainty for all cases except Rod R6 with the stoichiometric diffusivities. It has been determined that that predictions of low quantities of fission gas, as measured from these experiments, is exceptionally difficult and a factor of 10 is deemed acceptable at these low absolute values [44].

Figures 11 and 12 illustrate the Spearman correlation coefficients for the stoichiometric and Si-rich fission gas diffusivities respectively. Spearman correlation coefficients were chosen because some of the uncertain inputs have orders of magnitude variation. These coefficients can identify monotonic relationships between inputs and outputs and are always between -1.0 and 1.0. A larger negative value indicates that, as the uncertain input is increased, the corresponding output of interest decreases. Conversely, a larger positive value indicates a positive monotonic relationship between the input and output. A correlation value close to 0.0 indicates no monotonic relationship. A statistically significant relationship between an input and output is assumed to occur when the absolute value of the correlation coefficient is greater than 0.33.

It is observed that the trends between the Spearman correlation coefficients are the same whether or not the diffusivities used for the fission gas atoms and vacancies in the fission gas model are treated as stoichiometric or Si-rich. One sees a

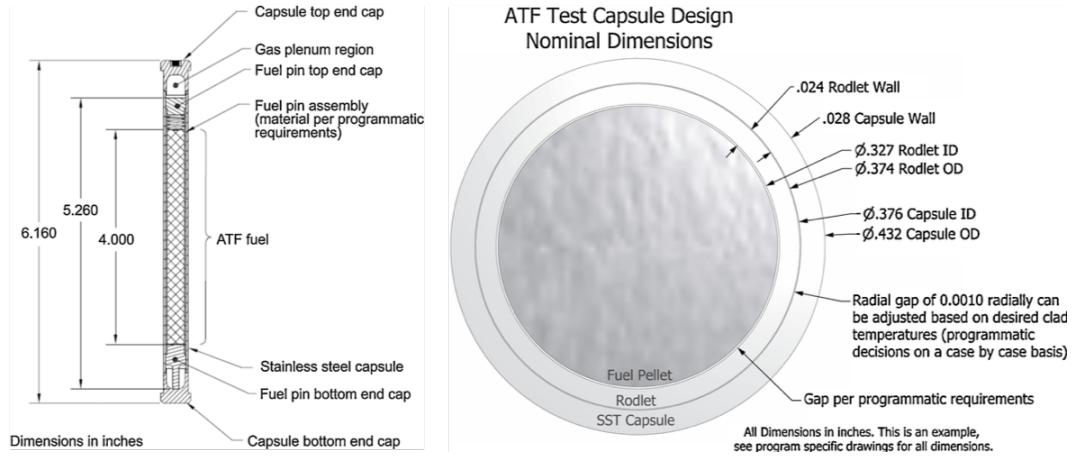


Figure 9: ATF-1 test capsule assembly (left) and capsule cross-section (right). Images reproduced from [40].

Table 4: Summary of  $U_3Si_2$  models available in BISON, including range of applicability, uncertainty, and the distribution used in the uncertainty quantification and sensitivity analyses of the validation cases.

| Model   | Range of Applicability                   | Uncertainty                                | References | Distribution |
|---|--|--|------------|--------------|
| Thermal conductivity                          | $13\text{ K} \leq T \leq 1500\text{ K}$  | $\pm 18.2\%$                               | [15]       | Normal       |
| Specific heat capacity                        | $293\text{ K} \leq T \leq 1500\text{ K}$ | $\pm 3\%$                                  | [15]       | Normal       |
| Young's modulus                               | $1.5\% \leq p \leq 10\%$                 | $\pm 29.1\%$                               | [15]       | Normal       |
| Poisson's ratio                               | $1.5\% \leq p \leq 10\%$                 | $\pm 26.8\%$                               | [15]       | Normal       |
| Thermal expansion                             | $273\text{ K} \leq T \leq 1473\text{ K}$ | $(16.0 \pm 3.0) \times 10^{-6}$            | [15]       | Normal       |
| Solid swelling                                | All burnups                              | $\pm 20\%$                                 | [24, 25]   | Normal       |
| Xe and vacancy diffusion thermal coefficients | Normal operating conditions              | Factor of 7.4                              |            | Uniform      |
| Xe and vacancy thermal activation energies    | Normal operating conditions              | $\pm 0.15\text{ eV}$                       |            | Uniform      |
| Xe and vacancy athermal coefficients          | Normal operating conditions              | Factor of 5                                |            | Uniform      |
| Fission gas release and gaseous swelling      | Normal operating conditions              | <sup>1</sup> Factor of $10^{-3}$ to $10^4$ | [42]       | Loguniform   |
|   | Normal operating conditions              | <sup>2</sup> Factor of 0.1 to 10           | [42]       | Uniform      |
|   | Normal operating conditions              | <sup>3</sup> $\pm 50\%$                    | [42]       | Uniform      |
|   | Normal operating conditions              | <sup>4</sup> Factor of $10^{-3}$ to $10^3$ | [42]       | Loguniform   |
|   | Normal operating conditions              | <sup>5</sup> Factor of 0.5 to 1            | [42]       | Uniform      |
|   | Normal operating conditions              | <sup>6</sup> $0.6 \pm 0.072$               | [42]       | Normal       |

<sup>1</sup>Applied to the nucleation factor of intra-granular bubbles. <sup>2</sup>Applied to the re-resolution rate of intra-granular bubbles. <sup>3</sup>Applied to the  $U_3Si_2$ /gas specific surface energy. <sup>4</sup>Applied to the initial number density of inter-granular bubbles. <sup>5</sup>Applied to the semi-dihedral angle of inter-granular bubbles. <sup>6</sup>Applied to the saturation coverage of grain boundaries.

moderate effect due to the power (and correspondingly temperature) differences between Rods R4 and R6 (e.g., thermal conductivity and the coefficient of thermal expansion). The most significant relationships with fuel elongation are possessed by the intra-granular nucleation factor, the vacancy diffusion activation energy, the solid swelling factor, the coefficient of thermal expansion, and the thermal conductivity. For fission gas release, the significant input parameters are the intra-granular nucleation factor, the vacancy diffusion activation energy, the inter-granular bubbles dihedral angle, and the intra-granular resolution rate. Performing additional lower length scale calculations or separate effects experiments for these parameters will help reduce the uncertainty in the inputs and correspondingly improve predictions of the outputs of interest.

## 6. Conclusions

Experimental data is limited on the behavior of  $U_3Si_2$  under irradiation at LWR operating temperatures. To address this issue, an effort to develop lower length scale informed models of  $U_3Si_2$  fuel behavior for use in the engineering was undertaken. This work summarized the recommended available models in the fuel performance code BISON, including the final form of the aforementioned lower length scale informed models. The range of applicability, uncertainty, and distributions assumed for uncertainty quantification and sensitivity analyses was provided. The development and determination of uncertainty of the models presented for thermal conductivity, specific heat capacity, thermal expansion, elasticity, and solid swelling was completed elsewhere [12]. The new features presented include the

Table 5: BISON comparisons to PIE data for ATF-13 R4 and ATF-15 R6 [45].

|                         | BISON          |                |                |                | Experiment |        |
|-------------------------|----------------|----------------|----------------|----------------|------------|--------|
|                         | R4             |                | R6             |                | R4         | R6     |
| Fuel elongation (mm)    | 0.099 to 0.163 | 0.088 to 0.154 | 0.135 to 0.223 | 0.112 to 0.225 | 0.0        | 0.0    |
| Fission gas release (/) | 0.0 to 0.007   | 0.0 to 0.002   | 0.0 to 0.014   | 0.0 to 0.011   | 0.0006     | 0.0006 |

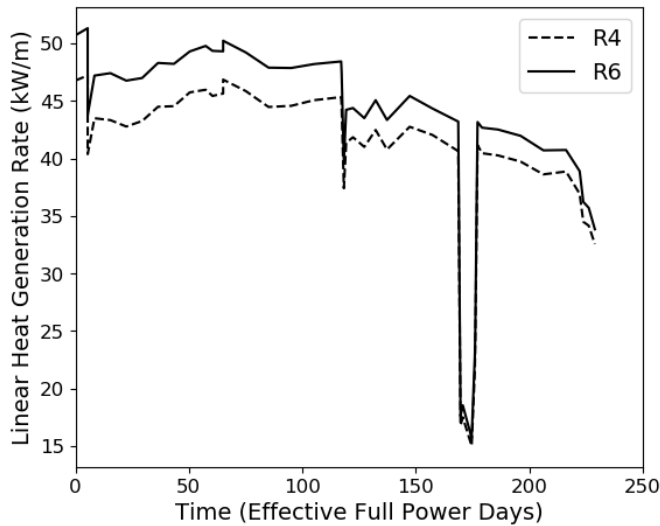


Figure 10: Linear heat generation rate supplied to ATR-13 R4 and ATR-15 R6. Adapted from [4].

lower length scale informed creep model and updates to the fission gas behavior model.

By using separate effects validation for empirical model development and the lower length scale calculations for more complicated fuel behavior, the validation to the only available integral rod tests could be performed. The main conclusions of this work are as follows:

- A multiscale modeling approach has been executed demonstrating its usefulness for analyzing fuel (or cladding) systems for which limited experimental data are available.
- Validation using the only available experimental data for LWR operating conditions was completed with good results for fission gas release and adequate results for fuel elongation.
- Fuel elongation comparisons did not match the experimental measurements within the range of uncertainty indicating that future work is necessary to derive a  $U_3Si_2$  densification model.
- The most sensitive parameters for fuel elongation calculations were the intra-granular nucleation factor, the vacancy diffusion activation energy, the solid swelling factor, the coefficient of thermal expansion, and the thermal conductivity.
- The most sensitive parameters for fission gas release calculations included the intra-granular nucleation factor, the

vacancy diffusion activation energy, the inter-granular bubbles dihedral angle, and the intra-granular re-solution rate.

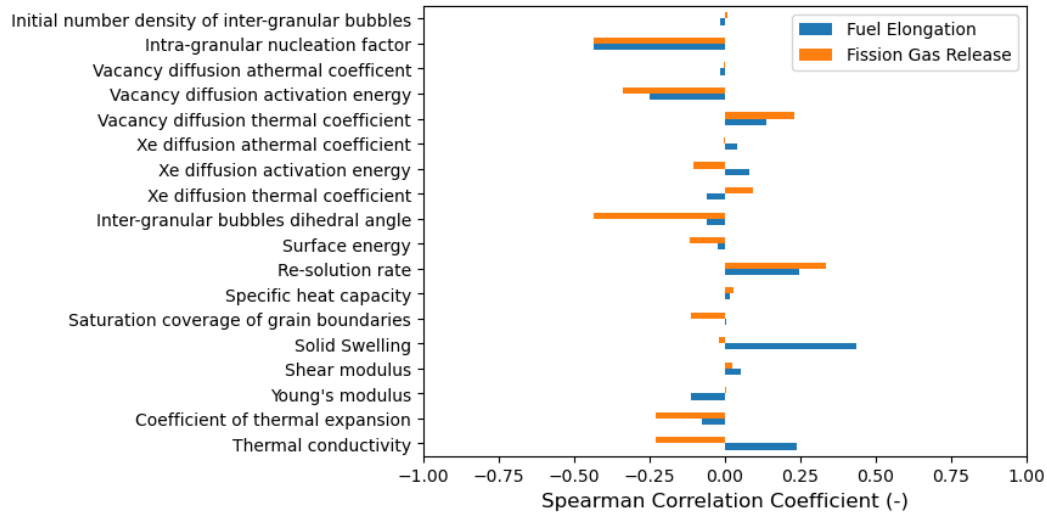
## 7. Acknowledgments

This work was funded by the US Department of Energy under both the Nuclear Energy Advanced Modeling and Simulation (NEAMS) and Consortium for Advanced Simulation of Light Water Reactors (CASL) programs. The submitted manuscript has been authored by a contractor of the U.S. Government under Contract DE-AC07-05ID14517. Accordingly, the U.S. Government retains a non-exclusive, royalty free license to publish or reproduce the published form of this contribution, or allow others to do so, for U.S. Government purposes.

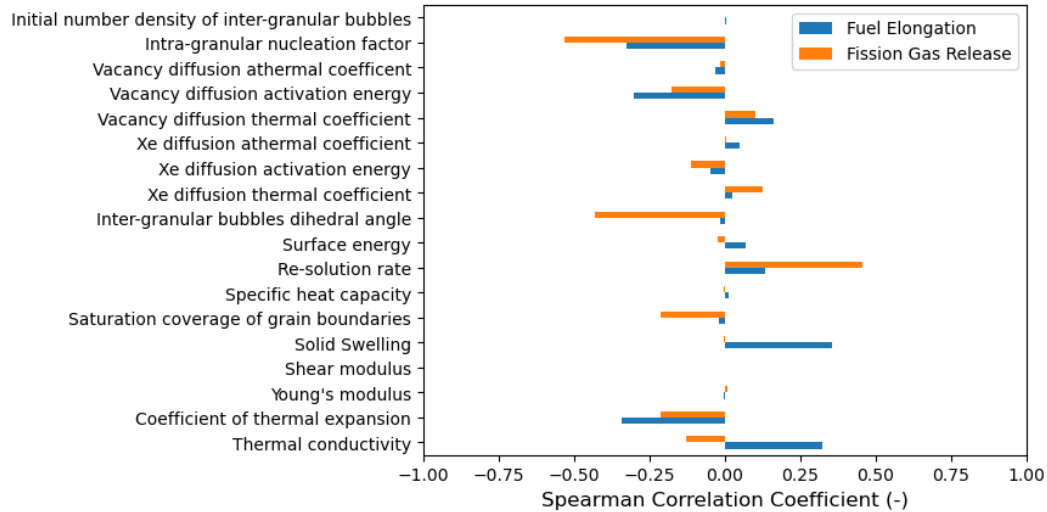
This research made use of the resources of the High Performance Computing Center at Idaho National Laboratory, which is supported by the Office of Nuclear Energy of the U.S. Department of Energy and the Nuclear Science User Facilities under Contract No. DE-AC07-05ID14517.

## References

- [1] S. Bragg-Sitton, B. Merrill, M. Teague, J. Ott, K. Rob, M. Farmer, M. Billone, R. Montgomery, C. Stanek, M. Tadesco, and N. Brown. Advanced fuels campaign light water reactor accident tolerant fuel performance metrics. Technical Report INL/EXT-13-29957, Idaho National Laboratory, 2014.
- [2] H. Shah, J. Romero, P. Xu, R. Oelrich, J. Walters, J. Wright, and W. Gassmann. Westinghouse-Exelon EnCore<sup>®</sup> Fuel Lead Test Rod (LTR) Program including Coated cladding Development and Advanced Pellets. In *Proceedings of TopFuel 2018*, 2018.
- [3] H. Shimizu. The properties and irradiation behavior of  $U_3Si_2$ . Technical Report NAA-SR-10621, Atomics International, 1965.
- [4] F. Cappia and J. M. Harp. Postirradiation examination of low burnup  $U_3Si_2$  fuel for light water reactor applications. *Journal of Nuclear Materials*, 518:62–79, 2019.
- [5] M. R. Finlay, G. L. Hofman, and J. L. Snelgrove. Irradiation behaviour of uranium silicide compounds. *Journal of Nuclear Materials*, 325:118–128, 2004.
- [6] R. C. Birtcher, J. W. Richardson, and M. H. Mueller. Amorphization of  $U_3Si_2$  by ion or neutron irradiation. *Journal of Nuclear Materials*, 230(2):158–163, 1996.
- [7] Y. Miao, J. Harp, K. Mo, S. Bhattacharya, P. Baldo, and A. M. Yacout. Short communication on "in-situ TEM ion irradiation investigations on  $U_3Si_2$  at LWR temperatures. *Journal of Nuclear Materials*, 484:168–173, 2017.
- [8] Y. Miao, J. Harp, K. Mo, S. Zhu, T. Yao, J. Lian, and A. M. Yacout. Bubble morphology in  $U_3Si_2$  implanted by high-energy Xe ions at 300°C. *Journal of Nuclear Materials*, 495:146–153, 2017.
- [9] Y. Miao, J. Harp, K. Mo, Y. S. Kim, S. Zhu, and A. M. Yacout. Microstructure investigations of  $U_3Si_2$  implanted by high-energy Xe ions at 600°C. *Journal of Nuclear Materials*, 2017.
- [10] R.L. Williamson, K.A. Gamble, D.M. Perez, S.R. Novascone, G. Pastore, R.J. Gardner, J.D. Hales, W. Liu, and A. Mai. Validating the BISON fuel performance code to integral LWR experiments. *Nuclear Engineering and Design*, 301:232 – 244, 2016.



(a)

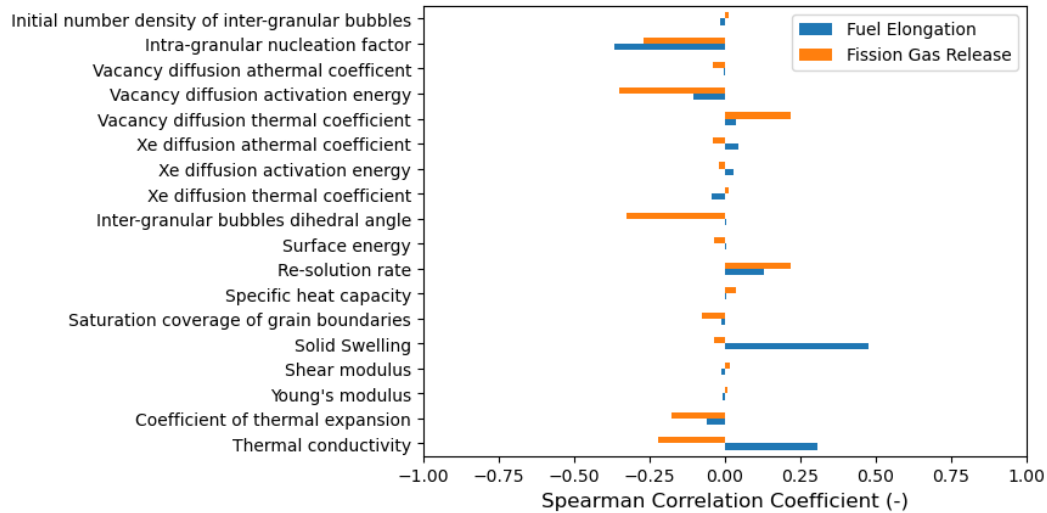


(b)

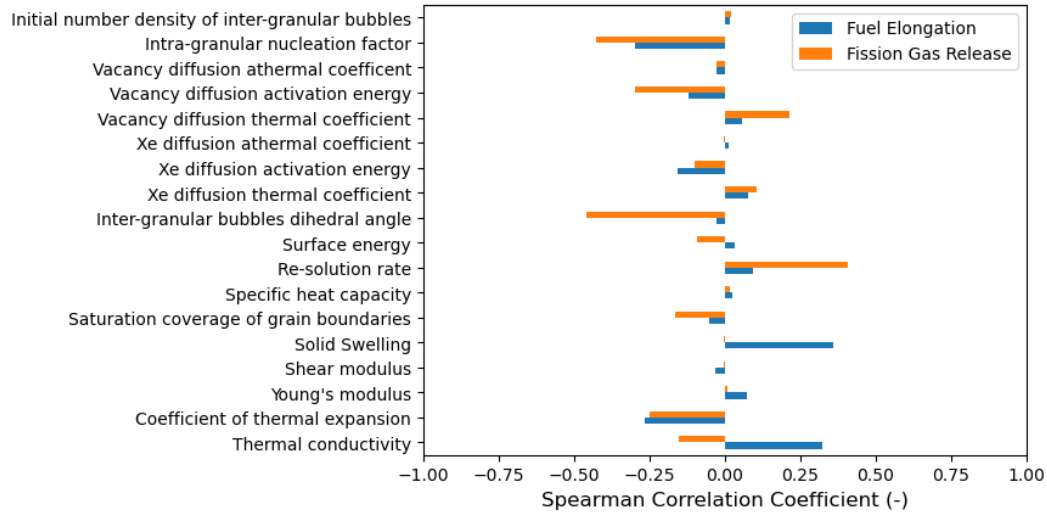
Figure 11: Spearman correlation coefficients using the stoichiometric diffusivities for (a) Rod R4 and (b) Rod R6.

- [11] T. Barani, G. Pastore, D. Pizzocri, D.A. Andersson, C. Matthews, A. Alfonsi, K.A. Gamble, P. Van Uffelen, L. Luzzi, and J.D. Hales. Multiscale modeling of fission gas behavior in  $U_3Si_2$  under LWR conditions. *Journal of Nuclear Materials*, 522:97–110, 2019.
- [12] K. A. Gamble, G. Pastore, M. W. D. Cooper, and D. Andersson. ATF material model development and validation for priority fuel concepts. Technical Report CASL-U-2019-1870-000 Rev.0, Idaho National Laboratory, 2019.
- [13] K. E. Metzger, T. W. Knight, and R. L. Williamson. Model of  $U_3Si_2$  fuel system using BISON fuel code. In *Proceedings of the International Congress on Advances in Nuclear Power Plants - ICAPP 2014*, Charlotte, NC, April 6–9 2014.
- [14] W. Li and K. Shirvan.  $U_3Si_2$ -SiC fuel performance analysis in BISON during normal operation. *Annals of Nuclear Energy*, 132:34–45, 2019.
- [15] J. T. White. Update to the  $U_3Si_2$  property handbook. Technical Report LA-UR-18-28719, Los Alamos National Laboratory, 2018.
- [16] J. T. White, A. T. Nelson, J. T. Dunwoody, D. J. Safarik, and K. J. McClellan. Corrigendum to Thermophysical Properties of  $U_3Si_2$  to 1773 K. *Journal of Nuclear Materials*, 484:386–387, 2017.
- [17] A. Mohamad, Y. Ohishi, H. Muta, K. Kurosaki, and S. Yamanaka. Thermal and mechanical properties of polycrystalline  $U_3Si_2$  synthesized by spark plasma sintering. *Journal of Nuclear Science and Technology*, 55(10):1141–1150, 2018.
- [18] D. Antonio, K. Shrestha, J. Harp, C. Adkins, Y. Zhang, J. Carmack, and K. Gofryk. Thermal and transport properties of  $U_3Si_2$ . *Journal of Nuclear Materials*, 508:154–158, 2018.
- [19] J. T. White, A. T. Nelson, J. T. Dunwoody, D. D. Byler, D. J. Safarik, and K. J. McClellan. Thermophysical properties of  $U_3Si_2$  to 1773K. *Journal of Nuclear Materials*, 464:275–280, 2015.
- [20] R. A. Freeman, T. Martin, E. Roberts, and T. W. Knight. Analysis of thermal creep for uranium silicide fuel using Bison. In *Proceedings of the 2018 International Congress on Advances in Nuclear Power Plants (ICAPP 18)*, Charlotte, NC, 2018.
- [21] K. E. Metzger. *Analysis of Pellet Cladding Interaction and Creep of  $U_3Si_2$  Fuel for use in Light Water Reactors*. PhD thesis, University of South Carolina, 2016.
- [22] E. A. C. Mercado. High temperature compression creep of  $u_3si_2$ . Master's thesis, University of South Carolina, 2018.
- [23] M. W. D. Cooper, K. A. Gamble, L. Capolungo, C. Matthews, B. Beeler, C. R. Stanek, and K. Metzger. Irradiation-enhanced diffusion and diffusion-limited creep in  $u_3si_2$ . *Journal of Nuclear Materials*, In Progress, 2021.
- [24] G. L. Hofman and W. S. Ryu. Detailed Analysis of Uranium Silicide Dispersion Fuel Swelling. Technical Report CONF-8909141–10, Argonne





(a)



(b)

Figure 12: Spearman correlation coefficients using the Si-rich diffusivities for (a) Rod R4 and (b) Rod R6.

- National Laboratory, 1989.
- [25] T. Ikonen and V. Tulkki. The importance of input interactions in the uncertainty and sensitivity analysis of nuclear fuel behavior. *Nuclear Engineering and Design*, 275:229–241, 2014.
- [26] D. A. Anderson, X.-Y. Liu, B. Beeler, S. C. Middleburgh, A. Claisse, and C. R. Stanek. Density functional theory calculations of self- and Xe diffusion in  $U_3Si_2$ . *Journal of Nuclear Materials*, 515:312–325, 2019.
- [27] C Matthews, R Perriot, M W D Cooper, C R Stanek, and D A Andersson. Cluster dynamics simulation of uranium self-diffusion during irradiation in  $UO_2$ . *Journal of Nuclear Materials*, 527:151787, 2019.
- [28] C Matthews, R Perriot, M W D Cooper, C R Stanek, and D A Andersson. Cluster dynamics simulation of xenon diffusion during irradiation in  $UO_2$ . *Journal of Nuclear Materials*, 540:152326, 2020.
- [29] S. Plimpton. Fast Parallel Algorithms for Short – Range Molecular Dynamics. *Journal of Computational Physics*, 117(June 1994):1–19, 1995.
- [30] B. Beeler, M. Baskes, D. Andersson, M. W. D. Cooper, and Y. Zhang. A modified Embedded-Atom Method interatomic potential for uranium-silicide. *Journal of Nuclear Materials*, 495:267–276, 2017.
- [31] B Beeler, D A Andersson, M W D Cooper, and Y Zhang. A molecular dynamics study of the behavior of Xe in  $U_3Si_2$ . *Journal of Nuclear Materials*, 523:413–420, 2019.
- [32] B. Beeler, M.W.D. Cooper, Z.-G. Mei, D. Schwen, and Y. Zhang. Radiation driven diffusion in  $\gamma U-Mo$ . *Journal of Nuclear Materials*, 543:152568, 2021.
- [33] M. W. D. Cooper, C. R. Stanek, J. A. Turnbull, B. P. Uberuaga, and D. A. Andersson. Simulation of radiation driven fission gas diffusion in  $UO_2$ ,  $ThO_2$  and  $PuO_2$ . *Journal of Nuclear Materials*, 481:125–133, 2016.
- [34] C Matthews, D Schwen, and A C Klein. Radiation re-solution of fission gas in non-oxide nuclear fuel. *Journal of Nuclear Materials*, 457:273–278, 2015.
- [35] S C Middleburgh, R W Grimes, E J Lahoda, C R Stanek, and D A Andersson. Non-stoichiometry in  $U_3Si_2$ . *Journal of Nuclear Materials*, 482:300–305, 2016.
- [36] G. Pastore, L. Luzzi, V. Di Marcello, and P. Van Uffelen. Physics-based modelling of fission gas swelling and release in  $uo_2$  applied to integral fuel rod analysis. *Nuclear Engineering and Design*, 256:75–86, 2013.
- [37] B. Beeler, M. Baskes, D. Andersson, M.W.D. Cooper, and Y. Zhang. Molecular dynamics investigation of grain boundaries and surfaces in  $U_3Si_2$ . *Journal of Nuclear Materials*, 514:290–298, 2019.
- [38] L. K. Aagesen, D. Andersson, B. W. Beeler, M. W. D. Cooper, K. A. Gamble, Y. Miao, G. Pastore, and M. R. Tonks. Phase-field simulations of intergranular fission gas bubble behavior in  $U_3Si_2$  nuclear fuel. *Journal of Nuclear Materials*, 541:152415, 2020.
- [39] J. M. Harp, P. A. Lessing, and R. E. Hoggan. Uranium silicide pellet



- fabrication by powder metallurgy for accident tolerant fuel evaluation and irradiation. *Journal of Nuclear Materials*, 466:728–738, 2015.
- [40] K. E. Barrett, K. D. Ellis, C. R. Glass, G. A. Roth, M. P. Teague, and J. Johns. Critical processes and parameters in the development of accident tolerant fuels drop-in capsule irradiation tests. *Nuclear Engineering and Design*, 294:38–51, 2015.
- [41] A. Cheniour, M. R. Tonks, B. Gong, T. Yao, L. He, J. M. Harp, B. Beeler, Y. Zhang, and J. Lian. Development of a grain growth model for  $U_3Si_2$  using experimental data, phase field simulation and molecular dynamics. *Journal of Nuclear Materials*, 532:152069, 2020.
- [42] T. Barani, G. Pastore, D. Pizzocri, D.A. Andersson, C. Matthews, A. Alfonsi, K.A. Gamble, P. Van Uffelen, L. Luzzi, and J.D. Hales. Multiscale modeling of fission gas behavior in  $U_3Si_2$  under LWR conditions. *Journal of Nuclear Materials*, 522:97–110, 2019.
- [43] B. M. Adams, L. E. Bauman, W. J. Bohnhoff, K. R. Dalbey, M. S. Ebeida, J. P. Eddy, M. S. Eldred, P. D. Hough, K. T. Hu, J. D. Jakeman, J. A. Stephens, L. P. Swiler, D. M. Vigil, and T. M. Wildey. Dakota, a multi-level parallel object-oriented framework for design optimization, parameter estimation, uncertainty quantification, and sensitivity analysis: Version 6.11 user’s manual. Technical Report SAND2014-4633, Sandia National Laboratories, 2019.
- [44] Giovanni Pastore, LP Swiler, Jason D Hales, Stephen R Novascone, Danielle M Perez, Benjamin W Spencer, Lelio Luzzi, P Van Uffelen, and Richard L Williamson. Uncertainty and sensitivity analysis of fission gas behavior in engineering-scale fuel modeling. *Journal of Nuclear Materials*, 456:398–408, 2015.
- [45] F. Cappia and J. M. Harp. Corrigendum to "postirradiation examination of low burnup  $U_3Si_2$  fuel for light water reactor applications". *Journal of Nuclear Materials*, 523:538, 2019.